The influence of the Interdecadal Pacific Oscillation on Temperature and Precipitation over the Globe

Bo Dong · Aiguo Dai

Abstract The Interdecadal Pacific Oscillation (IPO) is a 40–60 year quasi-oscillation seen mostly in the Pacific basin, but its impacts on surface temperature (T) and precipitation (P) have been found over Australia, the Southwest U.S. and other regions. Here, a global analysis of IPO's impacts on T and P and its modulation of ENSO's influence on T and P over the globe is performed using observational and reanalysis data and model simulations. Since 1920, there are two warm (1924–1944 and 1977–1998) and two cold (1945–1976 and 1999–present) IPO phases, whose change is associated with abrupt shifts in North Pacific sea level pressure (SLP) and contrasting anomaly patterns in T and P and atmospheric circulation over the eastern and western Pacific. The IPO explains more than half of the interdecadal variations in T and P over many regions, such as northeastern Australia, western Canada and northern India. Significant correlations between the IPO and local P are observed over eastern Australia, southern Africa and the Southwest U.S. The IPO also modulates ENSO's influence on local T and P over most of these regions. T over northern India is positively correlated with Niño3.4 ENSO index during cold IPO phases but the correlation turns negative or insignificant during IPO warm phases. Over northeastern Australia, the T versus ENSO and P versus ENSO correlations are stronger during the IPO cold phases than during the warm phases. The P versus ENSO correlation over southern Africa tends to be negative during IPO warm phases but becomes weaker or insignificant during IPO cold phases. The IPO-induced P anomalies can be explained by the associated anomaly circulation, which is characterized by a high SLP center and anti-cyclonic flows over the North Pacific, and negative SLP anomalies and increased wind convergence over the Indonesia and western Pacific region during IPO cold phases. These observed influences of the IPO on regional T and P are generally reproduced by an atmospheric model forced by observed sea surface temperatures.

Keywords Precipitation · Temperature · IPO · PDO · Pacific SST · Climate transition

1 Introduction

Interdecadal variability of the Pacific sea surface temperatures (SSTs) has been documented in numerous studies (e.g., Mantua et al. 1997; Zhang et al. 1997; Power et al. 1999; Deser et al. 2004; Dai 2013). Various indices (Deser et al. 2004) have been developed to quantitatively describe the ENSO-like multi-decadal climate variations, often referred to as the Pacific Decadal Oscillation (PDO; Mantua et al. 1997) or the Interdecadal Pacific Oscillation (IPO; Zhang et al. 1997; Power et al. 1999; Liu 2012; Dai 2013). The PDO and IPO are essentially the same interdecadal variability (Deser et al. 2004), with the PDO traditionally defined within the North Pacific while the IPO covers the whole Pacific basin. Although the exact mechanism behind the IPO (and PDO) is not well understood, current work

B. Dong · A. Dai (✉)
Department of Atmospheric and Environmental Sciences, University at Albany, State University of New York (SUNY), Albany, NY 12222, USA
e-mail: adai@albany.edu

B. Dong
e-mail: bdong@albany.edu

A. Dai
National Center for Atmospheric Research (NCAR), Boulder, CO, USA

(Liu 2012) suggests that the IPO (and PDO) results from changes in wind-driven upper-ocean circulation forced by atmospheric stochastic forcing and its time scale is determined by oceanic Rossby wave propagation in the extratropics.

The linkages between the IPO and interdecadal variations in surface temperature (T) and precipitation (P) have been found in many parts of the globe, including southwestern United States (Meehl and Hu 2006; Dai 2013), southern Africa (Reason and Rouault 2002), Indian monsoon region (Krishnan and Sugi 2003; Meehl and Hu 2006), Alaska (Hartmann and Wendler 2005; Bourne et al. 2010), western Canada (Kiffney et al. 2002; Verdon-Kidd and Kiem. 2009; Whitfield et al. 2010), the Sahel (Mohino et al. 2011), and eastern Australia (Verdon et al. 2004; Henley et al. 2013). Climate conditions in these regions show contrasting patterns during warm and cold phases of the IPO. For example, Hartmann and Wendler (2005) showed that during positive phases of the PDO, warmer and stormier climate occurs over Alaska as the result of the inshore advection of warm and moist air associated with a deeper Aleutian Low. Using a coupled climate model, Meehl and Hu (2006) simulated the decadal dry periods ("megadroughts") in the Southwest U.S. and Indian monsoon region, and attributed them to the multi-decadal SST variability in the Indian and Pacific Oceans that are linked to wind-forced ocean Rossby waves near 20°N and 25°S whose transit times set the decadal time scales. Dai (2013) showed that decadal precipitation variations over the Southwest U.S. closely follow the IPO since 1923, and the decadal precipitation variations were reproduced by an atmospheric model forced by observed SSTs. Lyon et al. (2013) showed that boreal spring precipitation over East Africa and many other land areas has changed abruptly around 1998/1999 when the IPO has apparently switched to a cold phase. While these previous studies have provided useful information on IPO's influence over various regions, a global analysis of IPO's influence on T and P using a consistent method and the same data source is still lacking.

When averaged globally, the IPO also modulates the global-mean temperature on decadal to multi-decadal time scales (Dai et al. 2015), although decadal to multi-decadal variations in North Atlantic SSTs may also play a significant role (DelSole et al. 2011; Wu et al. 2011; Muller et al. 2013; Tung and Zhou 2013). IPO's phase switch to a cold epoch around 1998/1999 is found to be a major cause of the recent slowdown in global warming rate (Kosaka and Xie 2013; Trenberth and Fasullo 2013; England et al. 2014; Dai et al. 2015). Thus, the IPO is a major source of decadal variability in global warming rate that is caused by internal climate variability, not external forcing (Dai et al. 2015).

The spatial patterns of the T and P anomalies associated with the IPO and ENSO are known to be broadly similar

(Deser et al. 2004). However, the interannual ENSO variability and its impacts on regional climate can be modulated by the IPO. For example, Gershunov and Barnett (1998) found that typical U.S. winter heavy precipitation and sea level pressure (SLP) patterns associated with El Niño are strong and consistent only during the positive phase of the PDO. Power et al. (1999) found that the relationship between ENSO and interannual climate variations over Australia is weak and insignificant during the warm phases of the IPO, but strong and significant when the IPO cools the SSTs in the tropical Pacific Ocean. Hu et al. (2013) reported that the interannual climate variability over the tropical Pacific Ocean was significantly weaker after 2000, when the mean state of the tropical Pacific is relatively cold after the phase switch of the IPO around 2000. King et al. (2013) found that La Niña events have larger influences on extreme rainfall over eastern Australia than El Niño events, and such asymmetry is enhanced during cold IPO epochs but nonexistent during warm IPO phases. Decadal modulation of ENSO's influence on local climate by the IPO is also found in South America (Garreaud et al. 2009; da Silva et al. 2011), Europe (Bice et al. 2012) and eastern United States (Goodrich and Walker 2011).

To provide a more complete view of IPO's impacts on T and P on decadal timescales and IPO's decadal modulation of ENSO's influence on regional T and P on multi-year timescales, here we present a global analysis using observational and reanalysis data and model simulations to identify all the regions with significant influences from IPO and examine IPO's decadal modulations over these regions. We also examine atmospheric circulation changes using IPO epoch difference maps. Compared with previous studies, our results provide a more complete global view of the IPO's influence on T and P and the associated atmospheric circulation patterns, thus improving our understanding of IPO's impact on global climate.

We first describe the data and method in Sect. 2. In Sect. 3, we first define an IPO index and its warm and cold epochs since 1920, and then examine the composite T and P anomalies for the IPO epochs, followed by regional analyses of the IPO's modulation of T and P and their teleconnection to ENSO. A summary is given in Sect. 4.

2 Data and method

We used the updated HadISST data set of gridded monthly SST from the UK Met Office (Rayner et al. 2003) to define the IPO. We focused on the period from 1920 to 2012 because SST observations are sparse over the tropical Pacific before around 1920. ENSO activities were quantified using monthly Niño3.4 (5°S–5°N, 120°W–170°W)

SST index derived by combining the index values before 1950 from NCAR (http://www.cgd.ucar.edu/cas/catalog/climind/TNI_N34/index.html#Sec5) and the index values since 1950 from NOAA (http://www.esrl.noaa.gov/psd/forecasts/sstlim/Globalsst.html). The Niño3.4 index data from NCAR were re-scaled to have the same mean as the NOAA data over a common period from 1950 to 2007, as done in Dai (2013). We computed annual SST anomalies, smoothed them using 3-year moving averaging to eliminate high-frequency variations, and then applied an empirical orthogonal function (EOF) analysis of the smoothed annual SST anomaly fields from 60°S to 60°N from 1920 to 2012 to define the IPO. The use of the near-global domain helps define and separate the leading global warming mode from the second IPO mode, and it confirms that the IPO mode is indeed concentrated primarily in the Pacific basin (Fig. 1a).
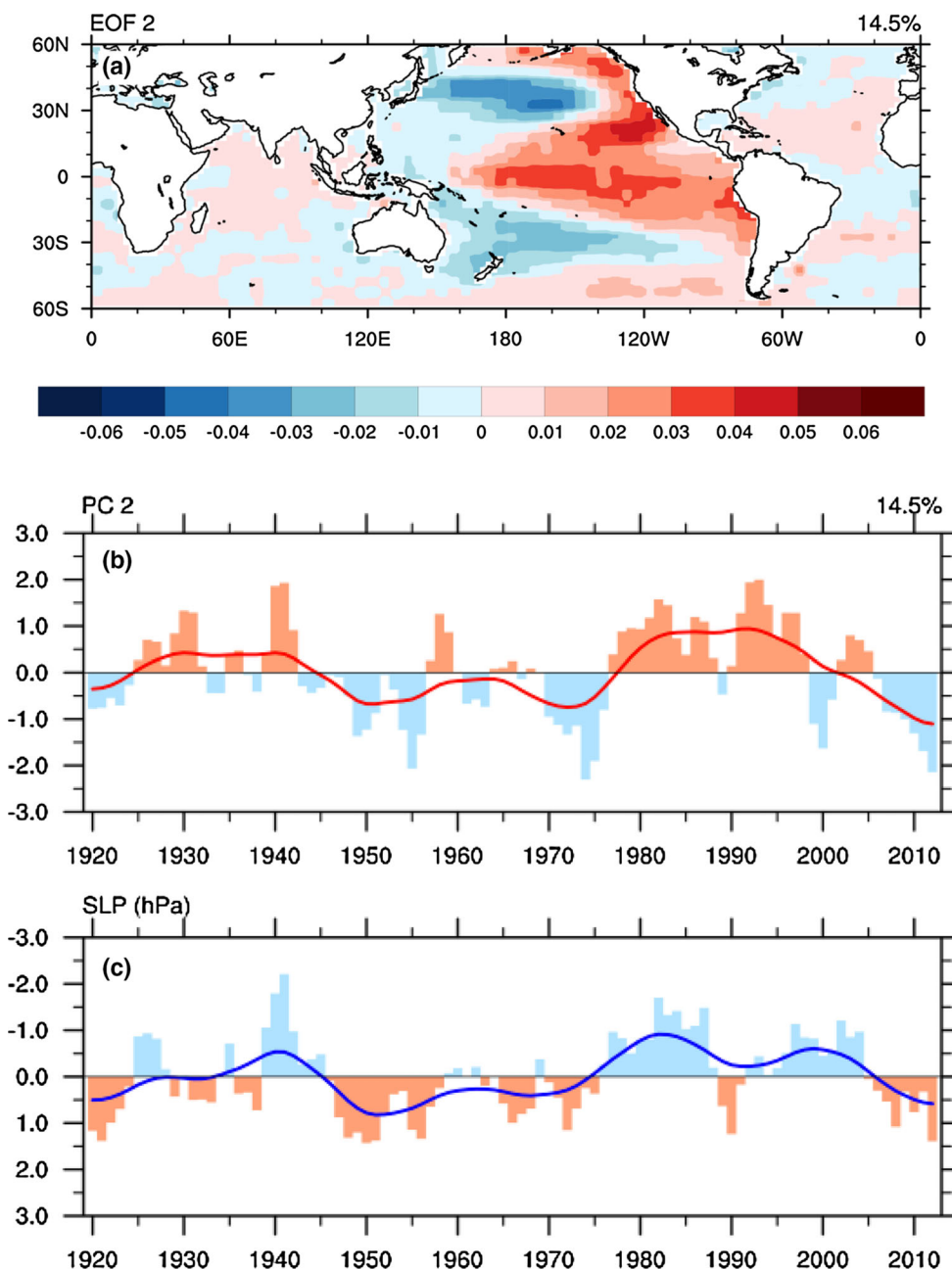
Fig. 1 a The second leading EOF of the 3-year moving averaged sea surface temperature from HadISST for 1920–2012 and 60°S–60°N, and b the time series of the associated principle component (PC, bars for annual data, the red curve is a smoothed time series obtained by applying a 9-year moving average twice to the annual bars). c Time series of 3-year moving averaged winter (November–March) sea level pressure (hPa, bars for yearly values) represented by the first leading EOF for the North Pacific (27.5°–72.5°N and 147.5°E–122.5°W). The blue curve is a smoothed time series obtained by applying a 9-year moving average twice to the bars

This also reveals the importance of the IPO mode in the global SST fields, which partly motivated this study. After the EOF analysis, 9-year moving averaging was applied twice to the principal component (PC) time series of the IPO mode in order to remove interannual and most decadal (<20 year) variations from multi-decadal changes associated with the IPO. To extend the IPO time series as back and as present as possible, the end data points were averaged using mirrored anomalies (e.g., PC for 2013 is the same as for 2011, and 2014 is the same as 2010, etc.), which were used by IPCC (2007) and appear to work well based on our visual examination (e.g., Fig. 1b).

We tested other filtering methods, including the 13, 15, 17, 19-year cutoff Lanczos low-pass filters (Duchon 1979). The results are similar to those reported in this paper, and all of these filtering methods were able to identify the positive and negative IPO phases shown by our IPO index (red curve in Fig. 1b). As in Dai (2013), we chose the 9-year moving averaging here in order to retain as many as possible the data points near the two ends, since most other filters with a similar cutoff period use a much longer data window, which greatly reduces the record length on the two ends of the data series. Our visual examination of Fig. 1b and comparisons with the IPO phase changes identified by Deser et al. (2004) suggests that our smoothed IPO index captures well the inter-decadal variations contained in the annual series and the correct timing for the IPO phase changes, although most decadal (<20 years) variations are smoothed out in our IPO index. Thus, our analysis focuses mainly on the inter-decadal (>20 years) variations from the Pacific, in contrast to many previous studies (e.g., Zhang et al. 1997; Power et al. 1999; Krishnan and Sugi 2003; Meehl et al. 2013), in which most decadal (10–20 year) variations were often retained.

Monthly precipitation (P) data over land from 1920 to 2010 were obtained from the Global Precipitation Climatology Centre (GPCC full v2.2, http://gpcc.dwd.de, Schneider et al. 2014). Monthly precipitation over the oceans since 1979 were obtained from the GPCP v2.2 data set (Huffman et al. 2009), which also was used to extend the GPCC land precipitation to 2012. Results using other precipitation data (e.g., those used by Dai 2013) are very similar and thus not discussed here. Gridded monthly data of surface air temperature (T) over land were obtained from the Climate Research Unit (CRUTEM4, http://www.cru.uea.ac.uk/cru/data/temperature/, Morice et al. 2012). We used the monthly sea level pressure (SLP) data for 1920–2012 from the twentieth Century Reanalysis (20CR, Compo et al. 2011). The 20CR SLP data were based on observations and obtained from NOAA (http://www.esrl.noaa.gov/psd/).

To minimize the effect of long-term trends on IPO composite anomalies, it is necessary to detrend the data, especially for T which contains a steady warming trend over most of the globe. We tried different methods that have been commonly used to detrend the data, including (1) removal of the linear trend at each grid point, (2) removal of the first EOF (global warming) mode of the observed T, and (3) removal of the component at each grid point associated with the global-mean T or P derived from the ensemble mean of 66 all-forcing historical climate simulations by 33 CMIP5 models (see Dai et al. 2015 for details). Method (1) assumes that the long-term trend induced by GHG, and other external forcing is linear, which is not true for T since the GHG and other historical forcings are known to vary with time. Method (2) for T is essentially the same as removing the component associated with the global-mean T series from observations since the first PC (PC1) closely resembles the global-mean T series (Dai et al. 2015). As shown by Dai et al. (2015), the global-mean T or the PC1 series includes the impacts of IPO and other natural modes, and it does not accurately reflect the GHG-induced warming trend since around 2000. Thus, method (2) yielded excessive warming over Northern Hemisphere land areas for the most recent IPO phase from 1999 to 2012 (not shown); otherwise, it yielded composite T anomalies similar to those using method (3) (see below). Method (3) was used in Dai et al. (2015) to separate the forced changes and unforced variations in global T fields. Although there are systematic biases, whose effect is minimized through the use of the regression equation between the model global-mean T series and local T series from observations, and other deficiencies in CMIP5 model simulations, the CMIP5 multi-model ensemble mean still represents our best estimate of the T and P response to GHG and other historical forcings. Thus, method (3) allows us to remove the forced long-term changes and focus on the internal variations. Here, we will only show results detrended using method (3) for T. For P data, we found that method (3) did not work well. Although the model ensemble-mean, global-mean P series follows the model global-mean T series, its upward trend since the 1950s leads to an apparent correlation with the IPO and Atlantic Multi-decadal Oscillation (AMO) indices during the recent decades, especially during 1979–2012, when global precipitation observations are available. As many precipitation records started after about 1950, this apparent correlation leads to the removal of a large portion of the IPO-induced variations from observed P series through the regression, because these IPO-induced inter-decadal variations appear to be a trend over a 30–50 year period and thus are correlated with the forced P trend from the models. This is less of an issue for detrending the T data, for which the record is longer and the forced signal is stronger. For SLP, trends in the global mean are small as air mass needs to be conserved. For these reasons, we simply detrended the P and SLP data using method (1).

For quantifying atmospheric circulation patterns associated with different IPO phases, we used the ERA-40 (for 1958–1978) and ERA-Interim (for 1979–2012; http://data.ecmwf.int/data/) reanalysis data. Before merging the two ERA products, the ERA-40 monthly data were rescaled so that the ERA-40 and ERA-Interim data have the same monthly climatology over the 1979–2001 common period. The reanalysis fields along with the observed temperature and precipitation data were averaged over different phases of the IPO to generate epoch composite maps. The statistical significance of the epoch composites was assessed by means of Student's t test.

To examine how precipitation and the atmosphere respond to observed SST forcing, we analyzed CanAM4 model simulations (on a T42 or $\sim 2.8°$ grid) done by the Canadian Centre for Climate Modelling and Analysis and made available through the CMIP5 data portals (http://pcmdi9.llnl.gov/esgf-web-fe/). These CanAM4 simulations contain four ensemble runs forced by observed SSTs from 1950 to 2009. The ensemble mean of these four runs was analyzed in this study.

Additionally, observed and model-simulated P and T were averaged over selected regions using grid-box area as the weight to form regional time series, which were further smoothed using the same method as that used for the IPO index, and then compared with the IPO index. For quantifying the decadal modulation by the IPO on ENSO's influence on regional T and P, we filtered the annual series of the Niño 3.4 SST index and the regional T or P series using a Lanczos filter (Duchon 1979) that removes variations on 13 year and longer time scales, and then computed the correlation coefficient between the high-passed ENSO index and the T or P series over a 13-year running window, as in Power et al. (1999). Results using the Southern Oscillation Index (SOI), instead of the Niño3.4 index, were similar and thus not discussed below. The statistical significance of the correlation is assessed by means of a Student's t test with autocorrelation being accounted for using the effective degree of freedom (Davis 1976; Zhao and Khalil 1993).

3 Results

3.1 IPO index and phase definition

Figure 1a, b shows the second EOF mode of near-global (60°S–60°N) SSTs from 1920 to 2012. As noticed previously (e.g., Zhang et al. 1997; Dai 2013), the "horse-shoe" shape of this EOF (Fig. 1a) exhibits ENSO-like SST patterns in the Pacific basin (Alexander et al. 2002) and PDO-like SST patterns in the North Pacific (Mantua et al. 1997). Further, this mode contains both ENSO-related multi-year

variations and decadal-to-multi-decadal oscillations. Here, we focus on the low-frequency multi-decadal variations represented by the smoothed red curve in Fig. 1b. Similar to Dai (2013), we will use this smoothed PC time series as an IPO index in our analysis. The exact timing of the IPO phase transitions depends on how the data series is smoothed and how the baseline (i.e., the zero-line in Fig. 1b) is defined. To be consistent with previous analyses (e.g., Deser et al. 2004; Dai 2013), we define two warm (or positive) IPO phases or epochs from about 1924 to 1945 and from 1977 to 1998, between which is a cold (or negative) phase from about 1946 to 1976. Since around 1999, the IPO has apparently switched to a cold phase as noticed previously (e.g., Ding et al. 2013; Jo et al. 2013; Dai 2013; Lyon et al. 2013), although the exact timing of this switch is complicated by the positive SST anomalies during 2002–2005 (Fig. 1b).

Figure 1c shows the boreal winter (November–March) SLP anomalies represented by the first leading EOF of the North Pacific (27.5°–72.5°N and 147.5°E–122.5°W) winter SLP fields. As shown by Deser et al. (2004), SST-based and North Pacific SLP-based indices are broadly consistent for the IPO phases, although subtle differences do exist, e.g., around 1945 and 2000 (Fig. 1b, c). In particular, the large La Niña event around 1999/2000, which is evident in the SSTs but absent in the North Pacific SLP, brings the most recent IPO phase shift a few years backward (red line in Fig. 1b) compared with the SLP-based index (blue line in Fig. 1c). It is unclear why the SLP in the North Pacific did not respond to the 1999/2000 La Niña event of the tropic Pacific. The SLP shifts around the year 1923/1924 and 1945/1946 generally agree with the SST-based IPO phase changes.

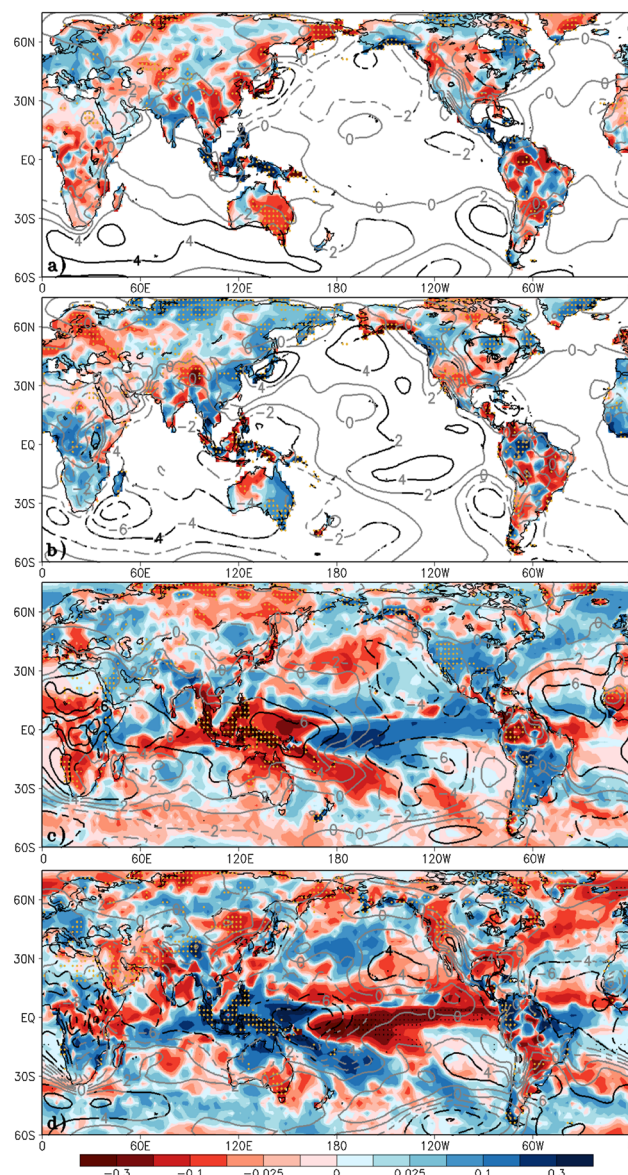## 3.2 Temperature and precipitation anomalies associated with IPO epochs

Phase changes of the IPO are expected to induce major climate shifts around the globe. For instance, the 1976/1977 IPO phase switch was coincident with the well documented North Pacific climate shift (e.g., Trenberth 1990; Yeh et al. 2011), and the recent 1998/1999 phase change is also associated with precipitation and other changes over many regions (Lyon et al. 2013). Here we examine the IPO epoch composite anomaly maps of T and P since 1920 to further quantify and compare the typical T and P anomalies associated with different IPO phases.

Figure 2 shows the IPO epoch anomalies of annual surface temperature, together with annual SLP anomalies (relative to the 1920–2012 mean). As expected, the SST anomaly patterns over the Pacific resemble the "horse-shoe" shape defined in Fig. 1a. The magnitude of the T anomalies is largest during 1977–1998, but comparable
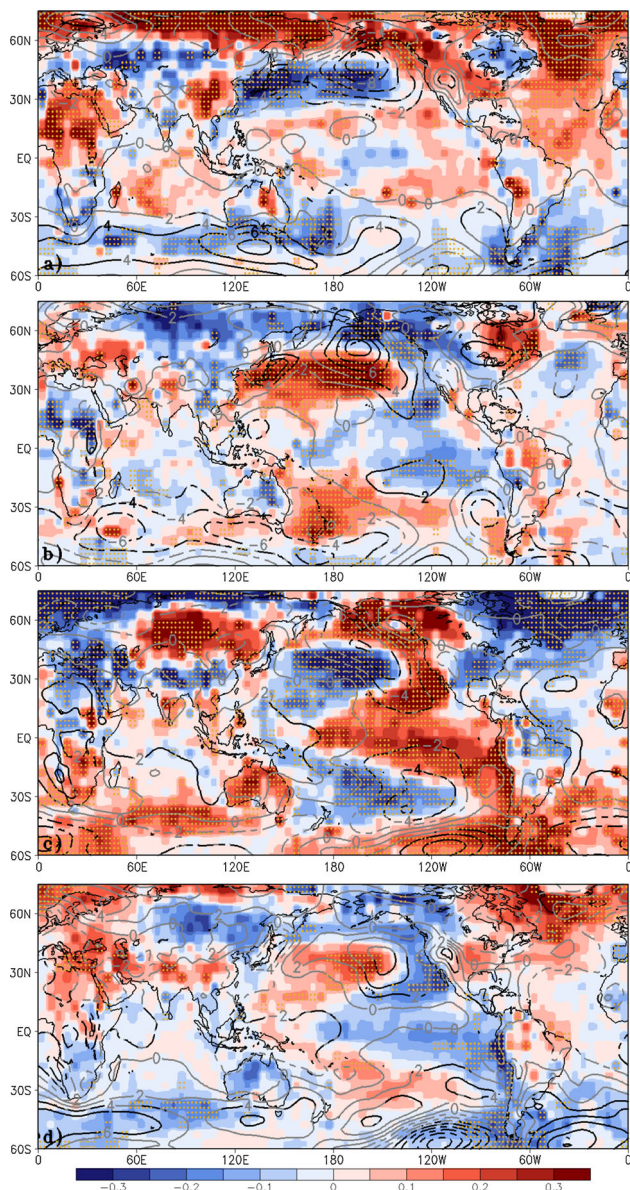
Fig. 2 IPO phase composite anomaly (relative to 1920–2012 mean) maps of the detrended annual surface air temperature (over land) and SST (over ocean) (*colors*, in °C) and annual SLP (contours, in 0.1 hPa and negative contours are dashed) for **a** 1924–1945, **b** 1946–1976, **c** 1977–1998, **d** 1999–2012. The *colored* areas with *dots* and *dark* contours are statistically significant at the 10 % level for the anomalies to be different from zero. The area-weighted global-mean values for panels **a**–**d** are, respectively, 0.014, −0.004, 0.017, and −0.017 °C. The T and SST data were detrended using method 3 while the SLP data were detrended using method 1 as described in Sect. 2

Fig. 3 Same as Fig. 2 but for epoch anomalies in annual precipitation (*colors*, in mm day^{-1}) for **a** 1924–1945, **b** 1946–1976, **c** 1977–1998, **d** 1999–2012. In *panel* (**c**) and (**d**), ocean precipitation anomalies are plotted using the GPCP v2.2 dataset, which begins in 1979. The SLP anomalies (contours) are in units of local standard deviation, different from Fig. 2

among the other epochs, except that the composite SST anomalies over the central and eastern tropical Pacific are relatively small during 1924–1945 (Fig. 2a). Some regional differences between Fig. 2a, c and between Fig. 2b, d (e.g., over Greenland and North Atlantic and northern Africa and the Mediterranean) likely result from influences from other

decadal modes such as the Atlantic Multi-decadal Oscillation (AMO), whose phasing differs from the IPO (Liu 2012; Dai et al. 2015). For the most recent warm (1977–1998) and cold (1999–2012) epochs, the T anomaly patterns are roughly the same with opposite signs. Given the stronger IPO amplitude (Fig. 1b) and more reliable data for these recent periods than the earlier epochs, the T anomaly patterns shown in Fig. 2c, d are likely to be more robust than those shown in Fig. 2a, b.

Figure 2c shows that during the warm IPO phase, SSTs in the central tropical Pacific and the whole eastern Pacific

from the Bering Strait to the Southern Ocean are 0.1–0.3 °C above normal, while SSTs in the western Pacific and the central North and South Pacific are 0.1–0.4 °C below normal. Surface T over the southern Indian Ocean, Australia, southern Africa, southern South America, Alaska and Pacific coastal North America, and midlatitude Asia are also 0.1–0.4 °C warmer than normal during the IPO warm phase, while it is 0.1–0.5 °C colder than normal over Greenland and the northern North Atlantic, Europe and northern Africa, and the central and eastern U.S. For the cold IPO phase from 1999 to 2012, the T anomalies have the opposite sign over the above regions but reduced magnitudes. Globally-averaged, the IPO, with contributions from other modes of climate variability such as the AMO (DelSole et al. 2011; Wu et al. 2011; Tung and Zhou 2013; Muller et al. 2013), enhances the global-mean T by 0.017 °C during 1977–1998 but reduces it by the same amount during 1999–2012. While these global-mean T anomalies are small, they can be substantially larger for shorter periods (5–15 years) (Dai et al. 2015). We emphasize that the magnitude of the estimated T anomalies depend on the baseline period used to compute the anomalies and also the T data set used in the analysis (see Dai et al. 2015 for more on this).

The composite anomaly patterns for precipitation (Fig. 3) are generally similar for warm and cold IPO phases but with opposite signs, although the P anomalies over some land areas (e.g., East Asia) are noisy and inconsistent between different phases (e.g., Fig. 3b, d). The large-scale P anomaly patterns from the Indonesia region to the North and South Pacific and from central-eastern tropical Pacific to the Atlantic Ocean (Fig. 3c, d) resemble the "horseshoe" patterns of precipitation anomalies induced by ENSO on multi-year timescales (Dai and Wigley 2000; Dai 2013). These P patterns are dominated by the dry (wet) condition over the Indonesia region during the warm (cold) IPO phases that extends northeast- and southeast-ward to the North Pacific and South Pacific, and the wet (dry) condition over the central and eastern tropical Pacific that also extends northeastward to the subtropical eastern North Pacific, the contiguous U.S. and the northern North Atlantic, and southeastward to the subtropical South Pacific, central and southern South America, and the southern South Atlantic (Fig. 3c, d). Precipitation over the Southern Ocean is also below (above) normal during the warm (cold) IPO phases (Fig. 3c, d). Precipitation over many other land areas is also affected by the IPO phases, although the P anomalies are noisy over land. For example, precipitation is generally below (above) normal during the warm (cold) IPO phases over eastern Australia, southern and West Africa, and northern Asia (Fig. 3).

Given the similar large-scale SST anomaly patterns for IPO and ENSO (Fig. 1a), these precipitation anomaly patterns can be explained by atmospheric circulation response to the SST anomalies (see Fig. 3 in Dai 2013). In the SLP field, the most robust feature is an anomalous low (high) over the central North Pacific and, to a lesser degree, also over the South Pacific during the warm (cold) IPO phases (Fig. 2). Over the tropical Pacific, SLP anomalies tend to be positive (negative) during the warm (cold) IPO phase over the western Pacific and Indonesia region, while they are the opposite in the eastern Pacific (Figs. 2, 3). These SLP anomalies weaken (enhance) the Pacific Walker circulation during the warm (cold) IPO phases, similar to that during the warm (cold) ENSO events. The composite circulation anomaly patterns are discussed below in more details.

3.3 Regional analysis of IPO's influence on T and P

To further examine the IPO's influence on T and P over land, we computed the correlation between the IPO index (red line in Fig. 1b) and similarly smoothed annual T and P anomalies (Fig. 4). Significant positive correlations between the IPO index and T are found over Alaska, western Canada and the western U.S., mid-latitude Asia, northern and central Australia, and parts of southern Africa (Fig. 4a), while negative correlations are seen over northeastern North and South America, and a band across the Mediterranean-Middle East-northern India (Fig. 4a).
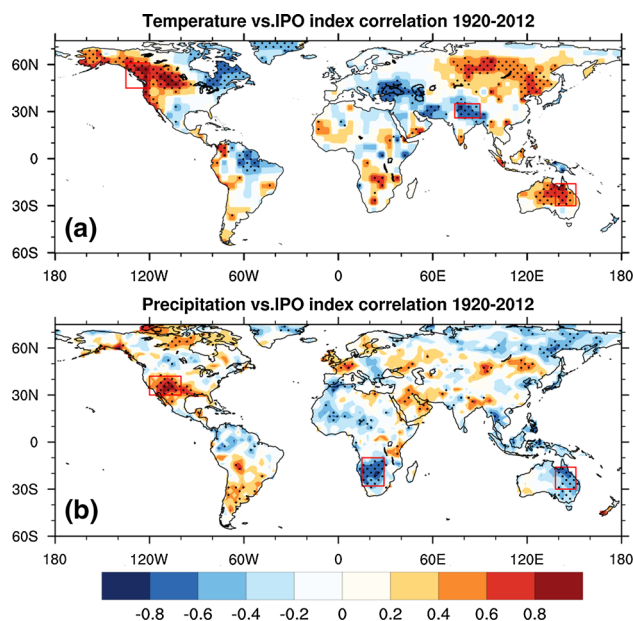

Fig. 4 Correlations between IPO index and smoothed annual temperature **a** and precipitation **b** for the period 1920–2012. *Colors* are correlation coefficients, and correlations that are statistically significant at 90 % confidence level are hatched. Same smoothing method for IPO index has been applied to the precipitation and temperature dataset before correlation analysis
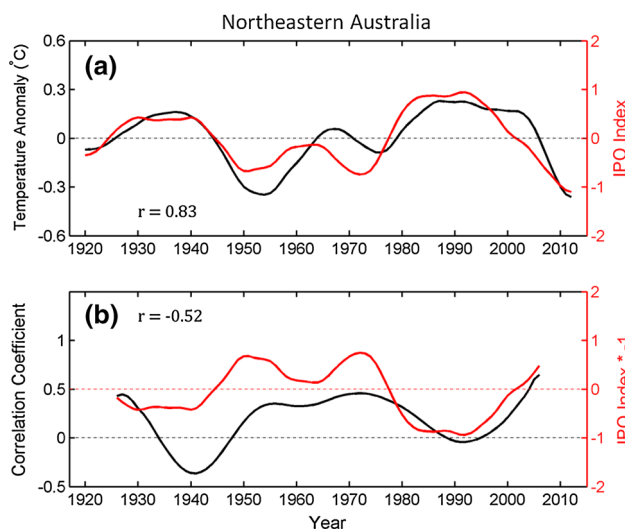
Fig. 5 a Time series of the smoothed annual surface temperature anomalies (*black line*) from 1920 to 2012 averaged over northeastern Australia (16–30°S, 138–151°E, land only), compared with the IPO index (*red line*) from Fig. 1b. The temperature anomalies are smoothed in the same way as the IPO index of Fig. 1b. b Time series of the smoothed correlation (*black line*) between the 13-year high-passed monthly Niño3.4 SST index and T anomalies over northeastern Australia over a 13-year running window. The smoothing of the correlation coefficient is the same as for the IPO index (*red line*). The correlation (r) between the two *curves* is also shown in both panels, and the r values are statistically significantly at the 10 % level (unless it has a superscript with an *asterisk*) based on a two-tailed Student *t* test with autocorrelation being accounted for

Consistent with Dai (2013), Fig. 4b shows that precipitation is positively correlated with the IPO index over the Southwest U.S., Argentina, and parts of Europe and Asia; while negative correlations exist over southern and West Africa, eastern Australia, Southeast and Northeast Asia. Figure 4 shows that the spatial patterns of the correlation with the IPO for T and P differ substantially. This suggests that the IPO's regional impacts on T and P are not the same over many land areas.

Based on the correlation maps, we selected five regions for further examination. They are outlined by the red boxes (land only) in Fig. 4, which include northeastern Australia (16–30°S, 138–151°E), western Canada (45–61°N, 120–135°W), northern India (26–35°N, 74–90°E), southern Africa (10–28°S, 15–29°E) and the Southwest U.S. (30–42°N, 100–120°W). We emphasize that the effective degree of freedom in the smoothed time series shown in Figs. 5, 6, 7, 8, 9, 10 are greatly reduced to around 14–22 for the correlation between the red and black lines and 10–18 for the correlation between the red and blue lines in these figures. Nevertheless, Student *t* test still showed that many of these correlations are statistically significant at the 10 % level (*p* value < 0.057 for all the correlations except for Figs. 6b, 10b).
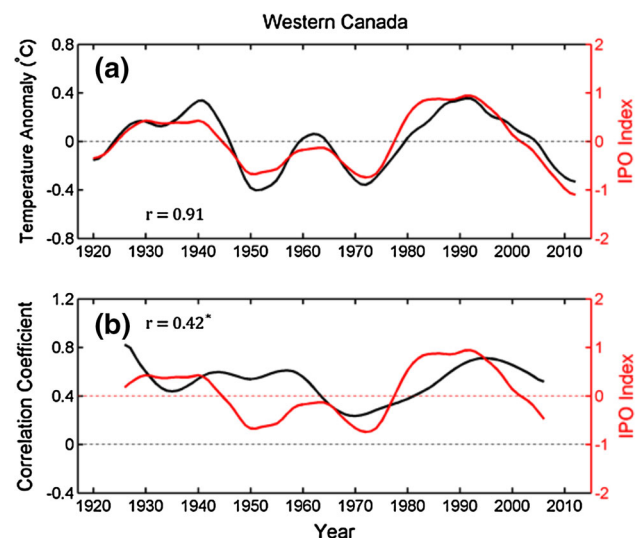
Fig. 6 Same as Fig. 5 but for western Canada (45–61°N, 120–135°W)
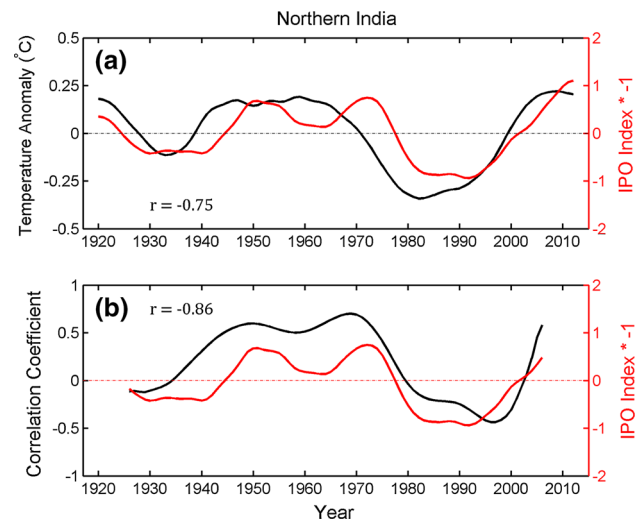
Fig. 7 Same as Fig. 5 but for northern India (26–35°N, 74–90°E)

Surface T over northeastern Australia (Fig. 5) shows significant positive correlation with the IPO index (r = 0.83), with the IPO explaining about 70 % of the decadal-to-multidecadal variability in T over this region. Surface T over northeastern Australia tends to be a few tenth of one degree Celsius warmer (colder) during the warm (cold) IPO phases such as 1924–1945 and 1977–1998 (1946–1976 and 1977–1998). Further, as noticed by Power et al. (1999), the IPO also modulates the ENSO-T correlation over Australia, with the high-pass filtered annual T versus Niño 3.4 SST correlation (*r*) being insignificant during most years of the warm IPO phases from 1924 to 1945 and 1977–1998 and positive (consistent with the decadal correlation shown in Fig. 5a) during IPO cold phases from 1947 to 1976 and 1999–2012. There is a
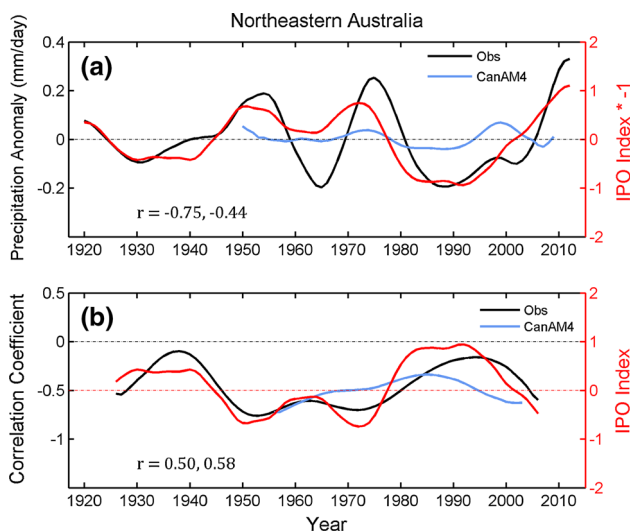
Fig. 8 Same as Fig. 5 but for IPO versus precipitation over northeastern Australia. The *blue line* in **a** is the similarly-smoothed precipitation from the CanAM4 model simulations forced by observed SSTs, while the *blue line* in **b** is the similarly-smoothed running correlation based on the model simulated precipitation. The *r* values in **a** are, from left to right, for the IPO index (*red*) versus observed P (*black*), and IPO index versus simulated P (*blue*) correlations. The *r* values in **b** are the correlation, from left to right, for the *red* versus *black curves*, and *red* versus *blue curves*
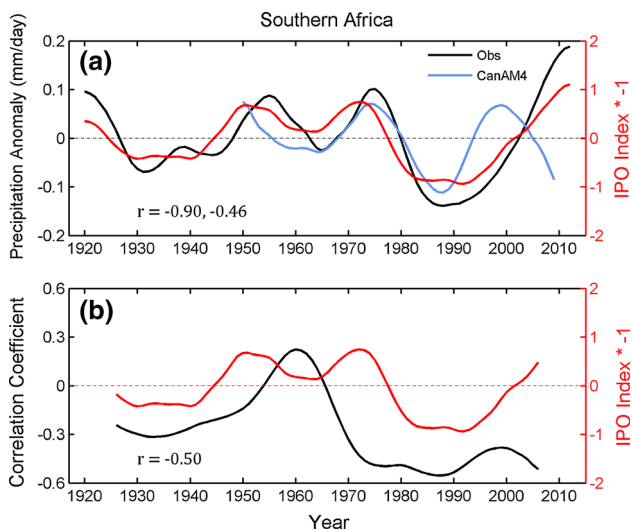
Fig. 9 Same as Fig. 5 but for IPO versus precipitation over Southern Africa. The *blue line* is the similarly-smoothed precipitation from the CanAM4 model simulations forced by observed SSTs. The r values in **a** are, from *left* to *right*, for the IPO index (*red*) versus observed P (*black*), and IPO index versus simulated P (*blue*) correlations

negative correlation of −0.52 between the *r* values and the IPO index (Fig. 5b). This suggests that the IPO not only influences decadal variations in northeastern Australian T, but also its connection to ENSO on multi-year time scales.

Strong positive correlation is also found between the IPO index and surface T over western Canada (r = 0.91),
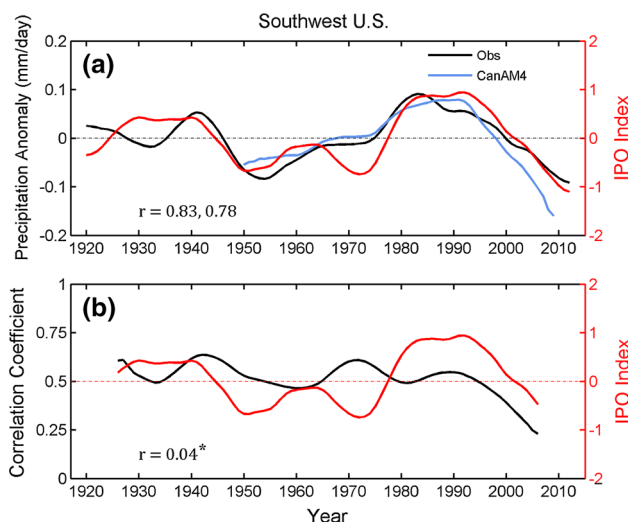
Fig. 10 Same as Fig. 9 but for the Southwest U.S (30–42°N, 100–120°W)

with T anomalies being about 0.1–0.3 °C warmer (colder) than normal during the IPO warm phases from 1924 to 1945 and 1977–1998 (cold phases from 1946 to 1976 and 1999–2012) (Fig. 6a). The T versus Niño3.4 SST correlation is also generally positive, and it is weakly correlated with the IPO index (r = 0.42; Fig. 6b). This suggests that the IPO has a strong influence on decadal variations in western Canadian T, but only a weak modulation of its connection to ENSO.

Over northern India, surface T is negatively correlated with the IPO (r = −0.75), with generally warmer T (by a few tens of 1 °C) during the peak cold IPO phases and colder T during the IPO warm phases (Fig. 7a). Further, Fig. 7b shows that the T versus ENSO correlation switches sign from positive (opposite to the correlation on decadal time scales shown in Fig. 7a) during 1936–1976 to negative and insignificant for the other years, and this decadal change is strongly correlated with the IPO index (r = −0.86). Thus, the IPO not only affects the T over northern India on multi-decadal time scales, but also strongly modulates its connection with ENSO on multi-year time scales.

Figures 8, 9 and 10 show similar regional series for annual P, with an additional blue line for model-simulated P for regions where the model was able to broadly reproduce the observed relationship. Over northeastern Australia, annual P tends to be 0.1–0.2 mm/day lower (higher) than normal during the IPO warm (cold) phases, with a correlation of −0.75 with the IPO index (Fig. 8a). The CanAM4 model qualitatively captures this negative correlation (r = −0.44) but with smaller P amplitudes. As expected, the correlation with ENSO is generally negative for northeastern Australian precipitation (Fig. 8b), which is consistent with the negative correlation with the IPO index

on decadal time scales but the opposite to the ENSO versus T correlation over this region (Fig. 5b). There is a significant positive correlation between the ENSO versus P correlation and the IPO index (r = 0.50), and this correlation is also seen in the CanAM4 model (r = 0.58, Fig. 8b).

The correlation between the IPO and southern African precipitation is even stronger than that over Australia, with r = −0.90 (Fig. 9a). Precipitation over southern Africa is lower (higher) by up to 0.1 mm/day during the warm (cold) IPO phases, such as 1924–1945 and 1977–1998 (1946–1976 and 1999–2012). The CanAM4 model roughly captures this negative correlation (r = −0.46). The correlation with ENSO is generally negative for southern African precipitation, but becomes weaker during the IPO cold phases (Fig. 9b).

For the Southwest U.S., our result (Fig. 10a) essentially reproduces Fig. 7b of Dai (2013), although we used a different precipitation data set. Figure 10b further shows that there is a positive correlation between ENSO and Southwest U.S. precipitation, which is consistent with the positive correlation with IPO on decadal time scales. Although the correlation with ENSO shows some decadal variations (e.g., weaker since the late 1990s), it is not correlated with the IPO index (Fig. 10b, time-lagged correlations are still insignificant), suggesting that the IPO does not modulate the P versus ENSO connection over the Southwest U.S.

We emphasize that the impact of the IPO on regional T or P and thus its correlation with them can vary with both its coupling strength (i.e., the T or P change per unit ENSO index) with the local T or P and the amplitude of the IPO index. Although a statistical analysis by van Oldenborgh and Burgers (2005) suggests a constant teleconnection strength of local P to an ENSO SST index, inter-decadal variations in the ENSO index (i.e., in the IPO index) can still induce inter-decadal variations in its impact on regional T or P, leading to correlations of the regional T or P with the IPO index, as shown here for some of the regions. To further check whether the decadal changes in the ENSO-T or ENSO-P correlations could arise by chance, we followed van Oldenborgh and Burgers (2005) method to assess the statistical significance of the decadal variations of the ENSO-T or ENSO-P correlation using 1,000 Monte Carlo simulations with synthetic T (or P) and Nino3.4 index (i.e., randomly sampled data from the observational series). The results suggested that the decadal variations of the ENSO-T or ENSO-P correlation is robust for all of our selected regions except northeastern Australia, where the decadal variation in the ENSO-T teleconnection could arise 29.2 % of the time by statistical fluctuations in the relatively short observational record. This test does not, however, address the correlation with

the IPO index, as is shown in the bottom panel of Figs. 5, 6, 7, 8, 9, 10.

3.4 Atmospheric anomaly circulations associated with the IPO

Using an atmospheric GCM, Kumar et al. (2001) showed that SST anomalies associated with the 1997 El Niño event over the globe and over the tropical central to eastern Pacific produce similar atmospheric anomaly circulations over the North Pacific and other regions that resemble observations. Other studies (e.g., Trenberth et al. 1998, 2002; Seager et al. 2003; Lin and Derome 2004) also suggest that tropical forcing associated with ENSO plays a dominant role in producing atmospheric anomaly circulation over the globe through Rossby wave teleconnection, meridonal-eddy transport, and heating anomalies associated with precipitation and cloudiness changes. There are also studies (e.g., Meehl and Hu 2006; Kosaka and Xie 2013) that suggest a similar dominant role of the tropical SSTs in forcing extratropical atmospheric anomaly circulation for IPO warm and cold phases. Thus, there is strong evidence that ENSO- or IPO-associated atmospheric anomaly circulations over the North Pacific and other extratropical regions are driven primarily by SST and other changes in the tropics. Here, we examine the IPO composite anomaly circulations and attempt to link them to the T and P anomaly patterns discussed above, with some discussions of their tropical origin mainly based on these previous studies. As shown by Dai (2013), the IPO composite anomaly circulations are strongest during the boreal cold season. Thus, we focus on the December–February (DJF) season here. Figure 11 shows the IPO cold-minus-warm epoch differences of DJF 850 hPa geopotential height (Z) and horizontal winds (U, V) from the ERA reanalyses, together with P over land. The overall Z patterns are similar to the SLP patterns shown in Fig. 2, but with stronger amplitudes. The epoch difference patterns for 1958–1976 minus 1977–1998 (Fig. 11b) are similar to the 500 hPa height patterns shown by Zhang et al. (1997) and Hartmann and Wendler (2005), although the time period of the cold and warm IPO phases defined in these studies are somewhat different.

The most prominent circulation anomalies appear over the North Pacific and are characterized by anticyclonic flows associated with an anomalous high, whose location varies slightly with IPO epochs (Figs. 2, 11). The high center is placed slightly south of the Aleutian Islands, and extends across a broad zonal band over the North Pacific, which reaches as west as Japan and as east as the Great Plains. These flow patterns indicate that during cold IPO phases such as 1946–1976 and 1999–2012, the anomalous high pressure system brings warm and moist air to Japan

Fig. 11 Epoch difference maps of DJF 850 hPa geopotential height (m, contours, *dashed lines* for negative values), winds (vectors, m s^{-1}) and precipitation (*colors*, in % of the 1979–1998 mean) for low-minus-high IPO regimes (years as indicated above each *panel*). The *dotted* areas and *black*-delineated contours and vectors represent statistically significant differences at the 10 % level. The geopotential height and wind data were from ERA-40 and ERA-interim reanalysis

(a) DJF 1999:2012 − 1977:1998 850hPa ΔZ,U;V,P(%)

(b) DJF 1958:1976 − 1977:1998 850hPa ΔZ,U;V,P(%)
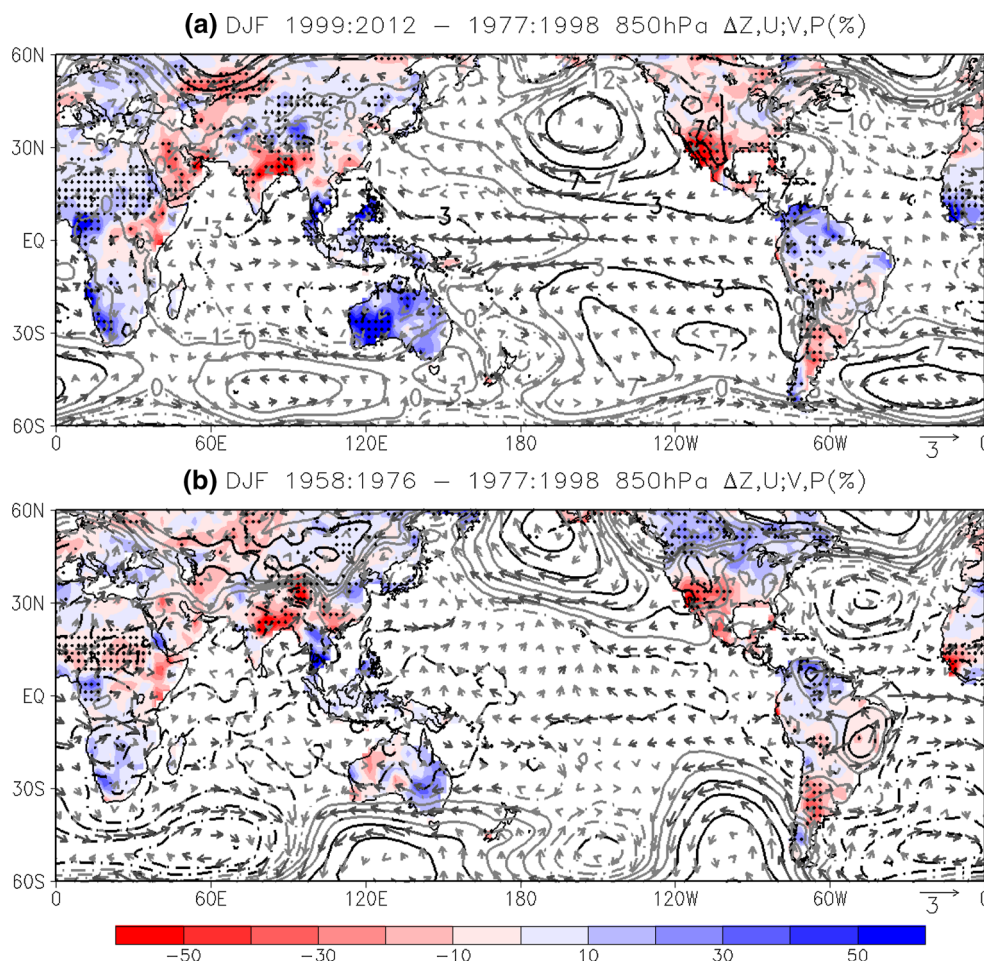
and northeast Asia, and advects cold and dry air into the Southwest U.S., leading to wet and dry conditions over these regions, respectively. These anomalous patterns roughly reverse during the warm IPO phases such as 1924–1945 and 1977–1998 (Fig. 2). According to Kumar et al. (2001), Seager et al. (2003), Lin and Derome (2004), and Meehl and Hu (2006), the SST-induced anomalous latent heating over the tropical Pacific produces atmospheric Rossby waves that affect atmospheric circulation over the North Pacific and other extratropical regions. Thus, the atmospheric anomaly circulation over the North Pacific (Figs. 2, 11) is likely to be a dynamic response to tropical latent heating induced by the SST anomalies associated with the IPO (Fig. 1a), with only secondary influences from extratropical SST changes.
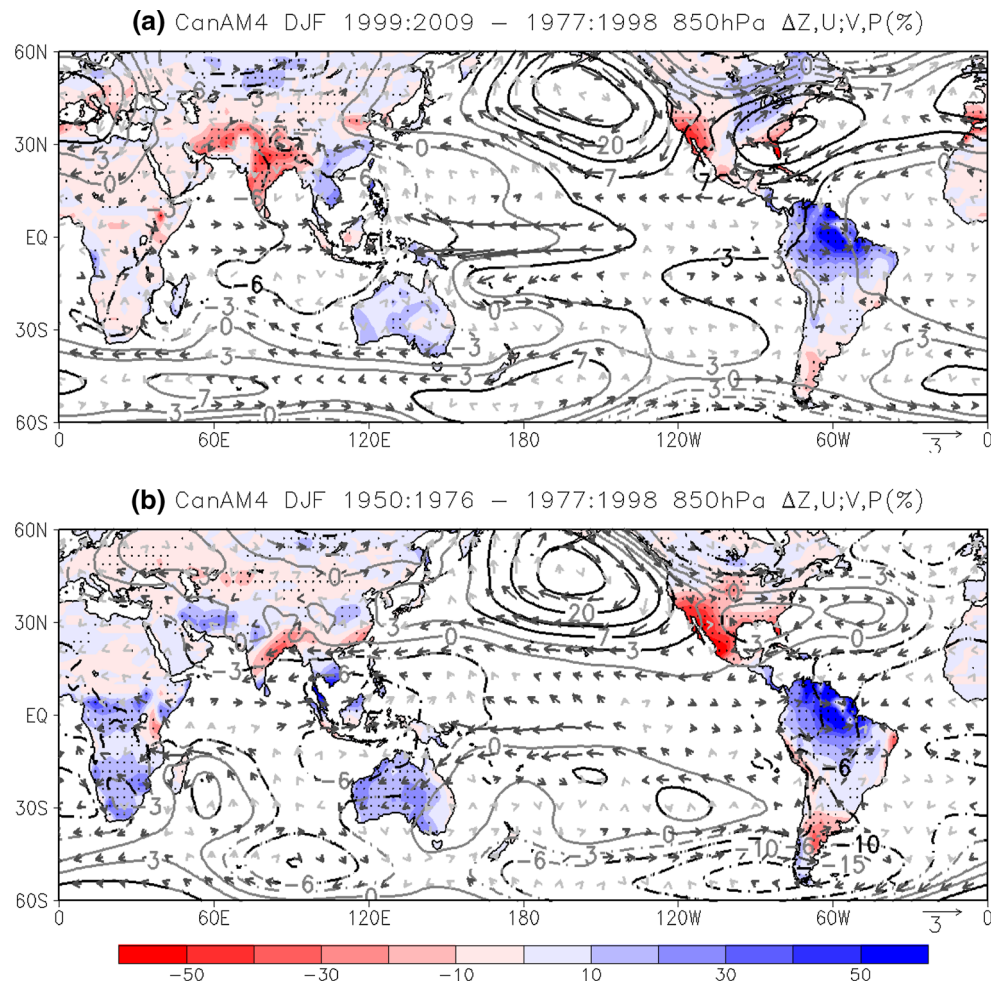
In the tropics, the Indonesia and western Pacific region has low pressure anomalies relative to the eastern Pacific during cold IPO phases (Figs. 2, 11), which is a response to the tropical SST changes (Fig. 1a). This enhances the Walker circulation over the Pacific and atmospheric convection in the Indonesia and western Pacific, leading to

increased precipitation over the maritime continent, including much of Australia. The situation is roughly reversed during warm IPO phases, with higher pressure over the western Pacific and reduced convection and precipitation over Australia (Fig. 3).

Over southern Africa, anomalous low (high) pressure tends to occur during cold (warm) IPO phases, leading to wet (dry) conditions during these periods (Figs. 2, 3, 11). These pressure and circulation anomalies over southern Africa appear to be part of the anomalous circulation patterns over the Southern Ocean that result primarily from the IPO-induced tropical forcing over the Pacific (Figs. 3, 11) (Kumar et al. 2001; Seager et al. 2003; Meehl and Hu 2006).

The CanAM4 model (Fig. 12) captures many of the features shown in Fig. 11. For example, the prominent height and wind anomaly patterns over the North Pacific resemble those in Fig. 11 for both epochs. They are also similar to the 500 hPa height patterns shown by Mantua et al. (1997), Zhang et al. (1997), and Hartmann and Wendler (2005). For both the negative IPO phases,

Fig. 12 Same as Fig. 11 but for DJF CanAM4 model outputs from 1950 to 2009, when its simulations ended

(a) CanAM4 DJF 1999:2009 − 1977:1998 850hPa ΔZ,U;V,P(%)

(b) CanAM4 DJF 1950:1976 − 1977:1998 850hPa ΔZ,U;V,P(%)

negative precipitation anomalies over the Southwest U.S. and upper Mexico are well reproduced by the model. For Australia and southern Africa, positive precipitation anomalies and the associated convergence circulations are well captured by the model for 1950–1976 but not for 1999–2009. Similar to reanalyses, atmospheric response to the IPO phase changes for the other seasons (not shown) are not as large as those for DJF.

The extra-tropical atmospheric response to IPO is further examined using the epoch difference of 200 hPa wave trains. Results (not shown) revealed noisy patterns, with the epoch difference statistically insignificant over many areas. Nevertheless, the general patterns (not shown) are similar to the wave response to the ENSO SST forcing (Trenberth et al. 1998; Dawson et al. 2011), with opposite anomalies over the eastern and western tropical Pacific and opposite anomalies to the higher latitudes at those longitudes. Thus, one may consider atmospheric response to IPO-associated SST anomalies follows similar processes seen during ENSO events, but occurs in decadal-multidecadal composites.

4 Summary and conclusions

To further quantify IPO's influences on surface temperature (T) and precipitation (P) over the globe, we have analyzed T, P, and SLP data from observations for 1920–2012, and atmospheric circulation fields from ERA reanalyses. We define the IPO as the second EOF mode of global (60°S–60°N) SST fields, using its smoothed principal component as the IPO index. Spatial SST patterns of the IPO are "ENSO-like", and "PDO-like" over the North Pacific. This low frequency climate mode approximately has a 40–60 year cycle, of which the phase reverses about every 20–30 years (Fig. 1b). From 1920 to 2012, there are roughly two warm IPO phases (1924–1945 and 1977–1998, with warm SSTs in the central and eastern tropical Pacific) and two cold IPO phases (1946–1976 and 1999–2012, with cold SSTs in the same region). The most recent cold IPO phase is still continuing.

We found that phase switches of the IPO are concurrent with major climate transitions over the globe, including abrupt shifts in SST, SLP, T and P. Besides the well

documented 1976/1977 climate shift associated with the IPO phase change (e.g., Trenberth 1990; Hartmann and Wendler 2005; Sabeerali et al. 2012), other IPO phase changes around 1945/1946 and 1998/1999 are also found to be associated with significant changes in SST, SLP, T and P over many regions, including many land areas. While the IPO composite T and P anomalies show a consistent horse-shoe pattern over the Pacific basin, T and P anomalies over extra-tropical land can be noisy and vary among different IPO phases (Figs. 2, 3). Nevertheless, T and P over many land areas are found to be significantly correlated with the IPO phase changes.

Annual surface air temperature is positively correlated with the IPO index (i.e., higher T during warming IPO phases such as 1924–1945 and 1977–1998) over western North America except its Southwest, mid-latitude central and eastern Asia, and central and northern Australia, but the correlation is negative over northeastern North America, northeastern South America, southeastern Europe, and northern India. Annual precipitation tends to be higher (lower) during warm (cold) IPO phases such as 1924–1945 and 1977–1998 (1946–1976 and 1999–2012) over south-western North America, northern India, and central Argentina, while it is the opposite over the maritime continent including much of Australia, southern Africa, and north-eastern Asia (Fig. 4b).

Besides the direct impacts on decadal variations in T and P, we also found some decadal modulations of ENSO's influence on T and P on multi-year timescales by the IPO over northeastern Australia, northern India, southern Africa and western Canada. Over northern India, T is positively correlated with Niño3.4 ENSO index during cold IPO phases but the correlation turns negative or insignificant during IPO warm phases. Over northeastern Australia, the T versus ENSO and P versus ENSO correlations are stronger during the IPO cold phases than during the warm phases. The P versus ENSO correlation over southern Africa tends to be negative during IPO warm phases but becomes weaker or insignificant during IPO cold phases. The T versus ENSO correlation over western Canada are generally positive, but tends to be weaker during IPO cold phases. During the most recent IPO cold phase, interannual climate variability over the tropical Pacific was found to be weak (Hu et al. 2013). This could potentially affect ENSO's influences on regional T and P. However, through what processes the IPO modulates ENSO's influence requires further investigation.

IPO composite maps of DJF SLP, 850 hPa height and winds show a large low-level high pressure center and anti-cyclonic flows over the North Pacific, and negative SLP anomalies and increased wind convergence over the Indonesia and western Pacific region during IPO cold phases such as 1946–1976 and 1999–2012. These anomaly circulation patterns are roughly reversed during the IPO warm phases such as 1924–1945 and 1977–1998. The anomaly wind and SLP patterns can qualitatively explain the observed precipitation anomalies over North America, Australia, southern Africa, and other regions. Distinct wave patterns are evident in the 200 hPa height composite map, which shows the extra-tropical response to the tropical height anomalies over the maritime continent and eastern Pacific, and their northeast- and south-east-ward propagation into the higher latitudes.

Many aspects of the observed relationships between the IPO and surface T and P, and the atmospheric circulation patterns are reproduced by the CanAM4 model forced with observed SSTs from 1950 to 2009. This suggests that the SST anomalies associated with the IPO are capable of producing the observed anomalies associated with the IPO in the T, P, and atmospheric circulation fields.

The regions with T and P being affected by IPO on decadal time scales generally resemble those influenced by ENSO on multi-year time scales (e.g., McBride and Nicholls 1983; Ropelewski and Halpert 1986; Dai and Wigley 2000; Giannini et al. 2008). Further, the IPO-composite circulation anomalies are also similar to those associated with ENSO events (Sarachik and Cane 2010). Thus, the IPO is an ENSO-like low-frequency mode not just in its SST and SLP patterns (Zhang et al. 1997), but also in its impacts on T and P and atmospheric fields. These results imply that many of the surface and atmospheric processes associated with ENSO also apply to the IPO phase changes, with the warm (cold) IPO phase resembling El Niño (La Niña). Our results also suggest that it is important to predict IPO's phase change for decadal climate predictions.

References

Alexander MA, Blade I, Newman M, Lanzante JR, Ngar-cheung L, Scott JD (2002) The atmospheric bridge: the influence of ENSO teleconnections on air–sea interaction over the global oceans. J Clim 15:2205–2231

Bice D, Montanari A, Vucetic V, Vucetic M (2012) The influence of regional and global climatic oscillations on Croatian climate. Int J Climatol 32:1537–1557

Bourne SM, Bhatt US, Zhang J, Thoman R (2010) Surface-based temperature inversions in Alaska from a climate perspective. Atmos Res 95:353–366

Compo GP et al (2011) The twentieth century reanalysis project. Q J R Meteorol Soc 137:1–28

da Silva GAM, Drumond A, Ambrizzi T (2011) The impact of El Nino on South American summer climate during different phases

of the Pacific Decadal Oscillation. Theor Appl Climatol 106:307–319

Dai A (2013) The influence of the inter-decadal Pacific oscillation on US precipitation during 1923–2010. Clim Dyn 41:633–646

Dai A, Wigley TML (2000) Global patterns of ENSO-induced precipitation. Geophys Res Lett 27:1283–1286

Dai A, Fyfe JC, Xie SP, Dai X (2015) Decadal modulation of global surface temperature by internal climate variability. Nature Clim Chang (to be accepted with minor revision)

Davis RE (1976) Predictability of sea surface temperature and sea level pressure anomalies over the North Pacific Ocean. J Phys Oceanogr 6:249–266

Dawson A, Matthew AJ, Stevens DP (2011) Rossby wave dynamics of the North Pacific extra-tropical response to El Niño: importance of the basic state in coupled GCMs. Clim Dyn 37:391–405

DelSole T, Tippett MK, Shukla J (2011) A significant component of unforced multidecadal variability in twentieth century global warming. J Clim 24:909–926

Deser C, Phillips AS, Hurrell JW (2004) Pacific interdecadal climate variability: linkages between the tropics and the North Pacific during boreal winter since 1900. J Clim 17:3109–3124

Ding H, Greatbatch RJ, Latif M, Park W, Gerdes R (2013) Hindcast of the 1976/77 and 1998/99 climate shifts in the Pacific. J Clim 26:7650–7661

Duchon CE (1979) Lanczos filtering in one and two dimensions. J Appl Met 18:1016–1022

England M et al (2014) Recent intensification of wind-driven circulation in the Pacific and the ongoing warming hiatus. Nat Clim Chang 4:222–227

Garreaud RD, Vuille M, Compagnucci R, Marengo J (2009) Present-day South American climate. Palaeogeogr Palaeoecol 281:180–195

Gershunov A, Barnett TP (1998) Interdecadal modulation of ENSO teleconnections. Bull Am Meteorol Soc 79:2715–2725

Giannini A, Biasutti M, Held IM, Sobel AH (2008) A global perspective on African climate. Clim Chang 90:359–383

Goodrich GB, Walker JM (2011) The influence of the PDO on winter precipitation during high- and low-index ENSO conditions in the eastern United States. Phys Geogr 32:295–312

Hartmann B, Wendler G (2005) The significance of the 1976 Pacific climate shift in the climatology of Alaska. J Clim 18:4824–4839

Henley BJ, Thyer MA, Kuczera G (2013) Climate driver informed short- term drought risk evaluation. Water Res Res 49:2317–2326

Hu ZZ, Kumar A, Ren HL, Wang H, L'Heureux M, Jin FF (2013) Weakened interannual variability in the tropical Pacific Ocean since 2000. J Clim 26:2601–2613

Huffman GJ, Adler RF, Bolvin DT, Gu G (2009) Improving the global precipitation record: GPCP version 2.1. Geophys Res Lett 36(17). doi:10.1029/2009GL040000

IPCC (2007) Climate change 2007: The physical science basis. Contribution of Working Group I to the fourth assessment report of the Intergovernmental Panel on Climate Change

Jo HS, Yeh SW, Kim CH (2013) A possible mechanism for the North Pacific regime shift in winter of 1998/1999. Geophys Res Lett 40:4380–4385

Kiffney PM, Bull JP, Feller MC (2002) Climatic and hydrologic variability in a coastal watershed of southwestern British Columbia. J Am Water Resour As 38:1437–1451

King AD, Alexander LV, Donat MG (2013) Asymmetry in the response of eastern Australia extreme rainfall to low-frequency Pacific variability. Geophys Res Lett 40:2271–2277

Kosaka Y, Xie SP (2013) Recent global-warming hiatus tied to equatorial Pacific surface cooling. Nature 501:403–407

Krishnan R, Sugi M (2003) Pacific decadal oscillation and variability of the Indian summer monsoon rainfall. Clim Dyn 21:233–242

Kumar A, Wang W, Hoerling MP, Leetmaa A, Ji M (2001) The sustained North American warming of 1997 and 1998. J Clim 14:345–353

Lin H, Derome J (2004) Nonlinearity of the extratropical response to tropical forcing. J Clim 17:2597–2608

Liu ZY (2012) Dynamics of interdecadal climate variability: a historical perspective. J Clim 25:1963–1995

Lyon B, Barnston AG, DeWitt DG (2013) Tropical Pacific forcing of a 1998–99 climate shift: observational analysis and climate model results. Clim Dyn. doi:10.1007/s00382-013-1891-9

Mantua NJ, Hare SR, Zhang Y, Wallace JM, Francis RC (1997) A Pacific interdecadal climate oscillation with impacts on salmon production. Bull Am Meteorol Soc 78:1069–1079

McBride JL, Nicholls N (1983) Seasonal relationships between Australian rainfall and the Southern Oscillation. Month Weather Rev 111:1998–2004

Meehl GA, Hu A (2006) Megadroughts in the Indian monsoon region and southwest North America and a mechanism for associated multidecadal Pacific sea surface temperature anomalies. J Clim 19:1605–1623

Meehl GA, Hu A, Arblaster JM, Fasullo J, Trenberth KE (2013) Externally forced and internally generated decadal climate variability associated with the Interdecadal Pacific Oscillation. J Clim 26:7298–7310

Mohino E, Janicot S, Bader J (2011) Sahel rainfall and decadal to multi-decadal sea surface temperature variability. Clim Dyn 37:419–440

Morice CP, Kennedy JJ, Rayner NA, Jones PD (2012) Quantifying uncertainties in global and regional temperature change using an ensemble of observational estimates: the HadCRUT4 dataset. J Geophys Res 117:D08101. doi:10.1029/2011JD017187

Muller RA, Curry J, Groom D, Jacobsen R, Perlmutter S, Rohde R, Rosenfeld A, Wickham C, Wurtele J (2013) Decadal variations in the global atmospheric land temperatures. J Geophys Res Atmos 118:5280–5286. doi:10.1002/jgrd.50458

Power S, Casey T, Folland C, Colman A, Mehta V (1999) Inter-decadal modulation of the impact of ENSO on Australia. Clim Dyn 15:219–324

Rayner NA, Parker DE, Horton EB, Folland CK, Alexander LV, Rowell DP (2003) Global analyses of sea surface temperature, sea ice, and night marine air temperature since the late nineteenth century. J Geophys Res 108:4407. doi:10.1029/2002JD002670

Reason CJC, Rouault M (2002) ENSO like decadal variability and South African rainfall. Geophys Res Lett 29:16-1-4. doi:10.1029/2002GL014663

Ropelewski CF, Halpert MS (1986) North American precipitation and temperature patterns associated with the El Niño/Southern Oscillation (ENSO). Month Weather Rev 114:2352–2362

Sabeerali CT, Rao SA, Ajayamohan RS, Murtugudde R (2012) On the relationship between Indian summer monsoon withdrawal and Indo-Pacific SST anomalies before and after 1976/1977 climate shift. Clim Dyn 39:841–859

Sarachik ES, Cane MA (2010) The El Niño-Southern Oscillation Phenomenon. Cambridge University Press, p 384

Schneider U, Becker A, Finger P, Meyer-Christoffer A, Ziese M, Rudolf B (2014) GPCC's new land surface precipitation climatology based on quality-controlled in situ data and its role in quantifying the global water cycle. Theor Appl Climatol 115:15–40

Seager R, Harnik N, Kushnir Y, Robinson W, Miller J (2003) Mechanisms of hemispherically symmetric climate variability. J Clim 16:2960–2978

Trenberth KE (1990) Recent observed interdecadal climate changes in the Northern hemisphere. Bull Am Meteorol Soc 71:988–993

Trenberth KE, Fasullo J (2013) An apparent hiatus in global warming? Earth Future 1:19–32

Trenberth KE, Branstator GW, Karoly D, Lau N-C, Ropelewski C (1998) Progress during TOGA in understanding and modeling global teleconnections associated with tropical sea surface temperatures. J Geophys Res 103:14291–14324

Trenberth KE, Caron JM, Stepaniak DP, Worley S (2002) Evolution of El Niño-Southern Oscillation and global atmospheric surface temperatures. J Geophys Res 107:4065. doi:10.1029/2000JD000298

Tung K-K, Zhou J (2013) Using data to attribute episodes of warming and cooling in instrumental records. PNAS 110:2058–2063

van Oldenborgh GJ, Burgers G (2005) Searching for decadal variations in ENSO precipitation teleconnections. Geophys Res Lett 32:L15701. doi:10.1029/2005GL023110

Verdon DC, Wyatt AM, Kiem AS, Franks SW (2004) Multidecadal variability of rainfall and streamflow: eastern Australia. Water Res Res 40:W10201

Verdon-Kidd DC, Kiem AS (2009) On the relationship between large-scale climate modes and regional synoptic patterns that drive Victorian rainfall. Hydrol Earth Syst Sci 13:467–479

Whitfield PH, Moore RD, Fleming SW, Zawadzki A (2010) Pacific Decadal Oscillation and the hydroclimatology of western Canada-review and prospects. Can Water Resour J 35:1–27

Wu Z, Huang NE, Wallace JM, Smoliak BV, Chen X (2011) On the time-varying trend in global-mean surface temperature. Clim Dyn 37:759–773

Yeh SW, Kang YJ, Noh Y, Miller AJ (2011) The North Pacific climate transitions of the winters of 1976/77 and 1988/89. J Clim 24:1170–1183

Zhang Y, Wallace JM, Battisti DS (1997) ENSO-like interdecadal variability: 1900–1993. J Climate 10:1004–1020

Zhao W, Khalil MA (1993) The relationship between precipitation and temperature over the contiguous United States. J Clim 6:1232–1240